Cai *et al. Energy Mater.* **2025**, *5*, 500038
DOI: 10.20517/energymater.2024.91

Energy Materials

Article

Open Access

Check for updates

Composition-regulated lattice strain of PdSn/C for boosting C1 pathway in ethanol electrooxidation

Yin Cai[1,#], Yi Tao[1,#], Jie Ding[2], Fuhua Li[3], Rongsheng Chen[1], Tao Ma[1,*], Feng Liang[1,*]

[1]The State Key Laboratory of Refractories and Metallurgy, School of Chemistry and Chemical Engineering, Wuhan University of Science and Technology, Wuhan 430081, Hubei, China.
[2]Department of Materials Science and Engineering, City University of Hong Kong, Hong Kong, SAR 999077, China.
[3]School of Chemistry and Chemical Engineering, Chongqing Key Laboratory of Theoretical and Computational Chemistry, Chongqing University, Chongqing 401331, China.
[#]Authors contributed equally.

***Correspondence to:** Dr. Tao Ma, The State Key Laboratory of Refractories and Metallurgy, School of Chemistry and Chemical Engineering, Wuhan University of Science and Technology, No. 947, Heping Avenue, Qingshan District, Wuhan 430081, Hubei, China. E-mail: taoma01@wust.edu.cn; Prof. Feng Liang, The State Key Laboratory of Refractories and Metallurgy, School of Chemistry and Chemical Engineering, Wuhan University of Science and Technology, No. 947, Heping Avenue, Qingshan District, Wuhan 430081, Hubei, China. E-mail: feng_liang@whu.edu.cn

How to cite this article: Cai, Y.; Tao, Y.; Ding, J.; Li, F.; Chen, R.; Ma, T.; Liang, F. Composition-regulated lattice strain of PdSn/C for boosting C1 pathway in ethanol electrooxidation. *Energy Mater.* **2025**, *5*, 500038. https://dx.doi.org/10.20517/energymater.2024.91

Received: 26 Jul 2024 **First Decision:** 23 Oct 2024 **Revised:** 11 Nov 2024 **Accepted:** 22 Nov 2024 **Published:** 24 Jan 2025

Academic Editors: Sining Yun, Hao Liu **Copy Editor:** Fangling Lan **Production Editor:** Fangling Lan

Abstract

The rational design of Pd-based catalysts to enhance their applications in ethanol oxidation reaction (EOR) presents both exciting opportunities and significant challenges. Herein, a series of carbon-supported PdSn nanoparticle catalysts (PdSn/C-X, X = 0.1, 0.5, 1, 2) with tunable lattice strains were synthesized using a facile method at room temperature and applied to the EOR. Our findings demonstrate that the activity and stability of EOR can be modulated by manipulating the lattice strain in Pd-based catalysts. Remarkably, PdSn/C-1 exhibits an excellent mass current density of 8,452.3 mA/mg_{Pd}, which is higher than that of most Pd-based catalysts, along with great stability, maintaining a mass activity of 573.9 mA/mg_{Pd} after 5,000 s. By combining structural analysis, *in situ* spectral characterization, and theoretical calculation, we elucidate that the optimal tensile strain adjusted by Sn composition in PdSn/C optimizes the free energy of the key intermediate (*CH_2CO) during EOR, thereby favoring the C1 pathway and enhancing catalytic activity. This study demonstrates that by controlling the composition, the lattice strain can be altered to improve catalytic performance of Pd-based catalysts in EOR.

Keywords: Pd-based catalysts, composition regulation, lattice strain, ethanol oxidation reaction, C1 pathway

INTRODUCTION

In recent years, direct ethanol fuel cells (DEFCs) have garnered significant attention due to their non-toxicity, high energy density (8 kWh/kg), and abundant ethanol sources[1-3]. However, the slow reaction kinetics and incomplete oxidation behavior of anodic ethanol oxidation reactions (EOR) hinder the commercialization of DEFCs[4,5]. EOR involves two pathways: complete oxidation (C1 pathway, involving 12 electrons transfer) and partial oxidation (C2 pathway, involving 2 or 4 electrons transfer)[6-10]. The C1 pathway offers a much higher energy density but is impeded by the high energy barrier associated with C-C bond cleavage and the slow desorption of CO-like species during oxidation[11]. Consequently, the C2 pathway predominates in practical applications, leading to poor DEFC efficiency[12]. Thus, developing high-efficiency catalysts that promote the C1 pathway by enhancing C-C bond cleavage and reducing CO poisoning during EOR is crucial for advancing DEFC technology.

To date, Rh- and Ir-based catalysts are known to favor the C2 pathway, but their scarcity, high costs, and low activity and selectivity for EOR limit their commercialization. Alternatively, Pd-based catalysts have shown promising performance due to their excellent catalytic activity[13,14]. However, Pd-based catalysts tend to favor the C2 pathway over the C1 pathway[15,16]. Surface strain engineering on Pd-based catalysts has emerged as an effective method to address this issue by adjusting the d-band properties[17-20], thus regulating the adsorption and desorption of key intermediates and shifting the balance toward the more efficient C1 pathway[8,21,22].

Research indicates that the tensile strain in Pd enhances EOR, while the compressive strain exerts the opposite effect[23]. A common strategy to create tensile strain involves preparing a core-shell structure, such as phosphorus-doped Ag@Pd catalysts, which show 19% selectivity for the C1 pathway due to the tensile strain from the differing lattice constants of Pd and Ag[11]. However, this strategy is limited by a complex multistep preparation process, making it difficult to simply regulate tensile strain. Additionally, Pd active sites are easily poisoned by CO-like intermediates, as they struggle to activate OH species, which are crucial for CO oxidation removal[11]. Previous studies have shown that doping Pd-based catalysts with oxyphilic metals enhances the removal of CO-like intermediates by facilitating the generation of OH species[24,25]. Thus, introducing oxyphilic atoms into Pd catalysts to regulate tensile strain and remove CO-like intermediates is a promising but underexplored approach.

Herein, we present our research on lattice strain-regulated activity of carbon-supported PdSn nanoparticles (NPs) catalysts for EOR, using a simple wet chemical method[26]. By adjusting the Sn content in PdSn NPs, we achieved various lattice strains in PdSn/C. PdSn/C-1, with an optimal tensile strain of 3.7%, demonstrated remarkable catalytic activity and enhanced stability compared to other Pd-based catalysts. The incorporation of oxyphilic Sn provides effective sites for the removal of CO-like species, improving the tolerance to CO-like intermediates. *In situ* attenuated total reflectance surface-enhanced infrared spectroscopy (ATR-SEIRAS) and density functional theory (DFT) calculations revealed that appropriate tensile strain in PdSn NPs significantly improves electrocatalytic activity by tuning the adsorption properties of key reaction intermediates (*CH_2CO) for further C-C bond cleavage. Our work introduces a novel strategy to modulate tensile strain in Pd-based catalysts for EOR through composition regulation and offers a comprehensive mechanism for EOR enhancement.

EXPERIMENTAL

Materials and reagents

Palladium chloride ($PdCl_2$) was obtained from Energy Chemistry. Stannous chloride ($SnCl_2$, 99.9%). Sodium citrate ($Na_3C_6H_5O_7 \cdot 2H_2O$, 99.9%), ethanol ($CH_3CH_2OH$, 99.7%), sodium borohydride ($NaBH_4$, 99.9%), and

potassium hydroxide (KOH) were provided by Shanghai Sinopharm Chemical Reagent Co., Ltd. Activated carbon (Vulcan XC-72) was sourced from Shanghai Macklin Biochemical Co., Ltd. Nafion solution (5 wt% in propanol and water) was purchased from Alfa Aesar. All reagents were of analytical grade and used without further purification. H_2O (18 MΩ) was purified using an ultra-pure purification system (HHitech, Eco-S15UF).

Preparation of PdSn/C catalysts

$PdCl_2$ (88 mg) was dissolved in 4.4 mL of water under magnetic stirring. Three drops of hydrochloric acid were added to adjust the acidity, and the mixture was left to stand for 2 h until complete dissolution was achieved. Then, 0.0948 g (0.5 mmol) of $SnCl_2$ and 2.358 g (8 mmol) of sodium citrate were added. Sodium citrate was used as a complexing agent to coordinate with Pd and Sn ions for uniform dispersion. The solution was diluted with 200 mL of water, followed by the addition of 200 mg of XC-72 with sonication for 30 min. Next, 50 mL of 0.1 M $NaBH_4$ was used as a reductant and injected into the mixture, followed by vigorous stirring at 25 °C for 8 h. The resulting suspension was centrifuged at 10,000 rpm for 5 min, and the supernatant was discarded. The sediment was washed with water and centrifuged three times. The collected product was dried in a vacuum oven at 60 °C for 5 h, resulting in the formation of PdSn/C-1. By varying the amounts of $SnCl_2$ (0.0316, 0.0474, and 0.1896 g), different PdSn/C catalysts were obtained, labeled as PdSn/C-0.1, 0.5, and 2, respectively. Additionally, as a control material, Pd/C was synthesized using the same procedure without adding $SnCl_2$.

Materials characterizations

Transmission electron microscopy (TEM, JEM-F200) and energy-dispersive X-ray spectroscopy (EDS, FEI Talos F200X) were employed to determine the morphology and chemical composition of the materials. X-ray powder diffraction (XRD) was performed using an X'Pert PRO MPD diffractometer with nickel-filtered Cu Kα radiation from Panalytical B.V. The Pd and Sn contents were measured using an inductively coupled plasma optical emission spectrometer (ICP-OES, Agilent 7700). The surface electronic states of the materials were identified using an X-ray photoelectron spectroscopy instrument (XPS, Thermo Scientific K-Alpha).

Electrochemical measurements

Electrochemical measurements were conducted using a three-electrode setup with an electrochemical workstation (AMETEK PARSTAT 4000A, Princeton). A glassy carbon electrode (GCE) with an internal area of 0.07068 cm^2 served as the working electrode. Platinum foil (2 cm × 2 cm) and saturated calomel electrode (SCE) were used as the counter and reference electrodes, respectively. All experiments were conducted at room temperature, and all applied potentials were referenced to the reversible hydrogen electrode (RHE) based on Nernst equation ($E_{RHE} = E_{SCE} + 0.244 + 0.0591 \times pH$), unless stated otherwise. For the preparation of ink solution, 1.4 mg of catalysts were dissolved in 1.4 mL of co-solvents (ethanol:water = 1:3, v/v) and sonicated for 30 min. Then, 28 μL of Nafion was added to the mixture, followed by additional sonication for 30 min. A working electrode with a loading amount of 200 μg/cm^2 was prepared by applying 5 μL of the ink solution onto the GCE and drying it at room temperature.

Electrochemical measurements were conducted between 0.27 and 1.47 V at a scan rate of 50 mV/s in N_2-saturated 1.0 M KOH or 1.0 M KOH + 1.0 M ethanol electrolyte. The electrochemically active surface area (ECSA) was calculated from the cyclic voltammetry (CV) curves in the PdO reduction peak region using $ECSA = Q_{PdO}/(0.405\ mC/cm^2 \times m_{Pd})$, where Q_{PdO} is the charge obtained by integrating the reduction peak area from PdO to Pd, 0.405 mC/cm^2 represents the charge required for the reduction of the monolayer PdO, and m_{Pd} is the mass of Pd on the working electrode (based on ICP-OES analysis, Supplementary Table 1). CO stripping experiments were conducted in N_2-saturated 1.0 M KOH solution after bubbling CO for

20 min at a potential of 0.27 V. To remove dissolved CO, high-purity N_2 was bubbled into the CO-saturated electrolyte for 20 min. CO stripping curves were recorded at a scan rate of 50 mV/s between 0.27 and 1.47 V.

In situ ATR-SEIRAS characterization

A three-electrode cell was employed for all SEIRAS tests, with a GCE, Ag/AgCl, and carbon rod as the working, reference, and counter electrodes, respectively. EOR measurements were conducted in an electrolyte of 1.0 M KOH + 1.0 M ethanol under N_2-saturated solution. The background spectrum was collected at 0.5 V while the potential was swept from 0 to 1.3 V.

Theoretical calculation methods

The DFT calculations were performed using the Vienna Ab Initio Simulation Package (VASP 6.3.0)[27]. The Perdew-Burke-Ernzerhof (PBE) functional was employed within the generalized gradient approximation (GGA) framework to compute the electronic exchange-correlation energy[28]. The projector augmented wave (PAW) method was used to describe the ion-electron interactions[29]. The structure was fully optimized using a conjugate gradient optimization technique, with a cutoff energy of 450 eV for the plane-wave basis set. A 3 × 3 × 1 Monkhorst-Pack grid was employed during structural optimization. The maximal force on each atom was set to be less than 0.02 eV/Å, with an energy change convergence criterion of less than 1×10^{-5} eV. The DFT-D3 semi-empirical correction was applied using Grimme's scheme. The Gibbs free energy change (ΔG) was defined for each elementary step as $\Delta G = \Delta E + \Delta ZPE - T\Delta S$, where ΔE is the adsorption energy from DFT calculations, ΔZPE is the zero-point energy correction, T is the temperature, and ΔS is the entropy change.

RESULTS AND DISCUSSION

Material synthesis and characterization

We synthesized a series of PdSn NPs supported on activated carbon, labeled as PdSn/C-X (X = 0.1, 0.5, 1, 2, representing the Sn/Pd molar ratio in the precursor), using a straightforward co-reduction process at room temperature [Figure 1A]. TEM images [Figure 1B-F] reveal that the PdSn NPs (indicated by the white dotted circles) are uniformly distributed on the carbon support without aggregation. Additionally, statistical analysis of 100 well-distributed Pd and PdSn NPs indicates an average particle size ranging from 3.0 to 4.0 nm [Supplementary Figure 1]. EDS mappings [Supplementary Figure 2] show that the Pd and Sn elements are well distributed within the NPs, confirming the bimetallic structure of the PdSn/C-X catalysts. As measured by means of ICP-OES [Supplementary Table 1], the results confirm that the Sn contents in PdSn/C-0.1, 0.5, 1, and 2 are 1.17, 1.26, 2.11, and 3.59 wt%, respectively, verifying the tunable composition of the PdSn/C catalysts.

To gain further insight into the surface structure of PdSn/C-X, we employed aberration-corrected high-angle annular dark-field scanning transmission electron microscopy (HAADF-STEM) and XRD. HAADF-STEM images at the atomic level [Figure 2A] show the lattice spacing of PdSn NPs, which were measured from the cyan line region covering ten planes. The lattice distances of the Pd/C and PdSn/C-0.1, 0.5, 1, and 2 catalysts were measured to be 2.16, 2.17, 2.19, 2.24, and 2.28 Å, respectively, corresponding to the (111) lattice plane of Pd[24]. Additionally, a lattice spacing of 2.91 Å was observed in PdSn/C-2, indicating the presence of the PdSn (111) phase in this sample[30]. It is worth emphasizing that the observed increase in the interplanar spacing indicates the presence of tensile strain resulting from the incorporation of Sn (which has a larger parameter compared to Pd) into the Pd lattice[31], as will be further supported by the XRD investigation. Furthermore, we defined the tensile strain as $(d_p-d_s)/d_s$, where the d_p represents the interplanar spacing of the doped sample, and d_s indicates the interplanar spacing of the pure reference sample[32]. We therefore approximated the tensile strains of 0.46%, 1.39%, 3.7%, and 5.6% for the surfaces of

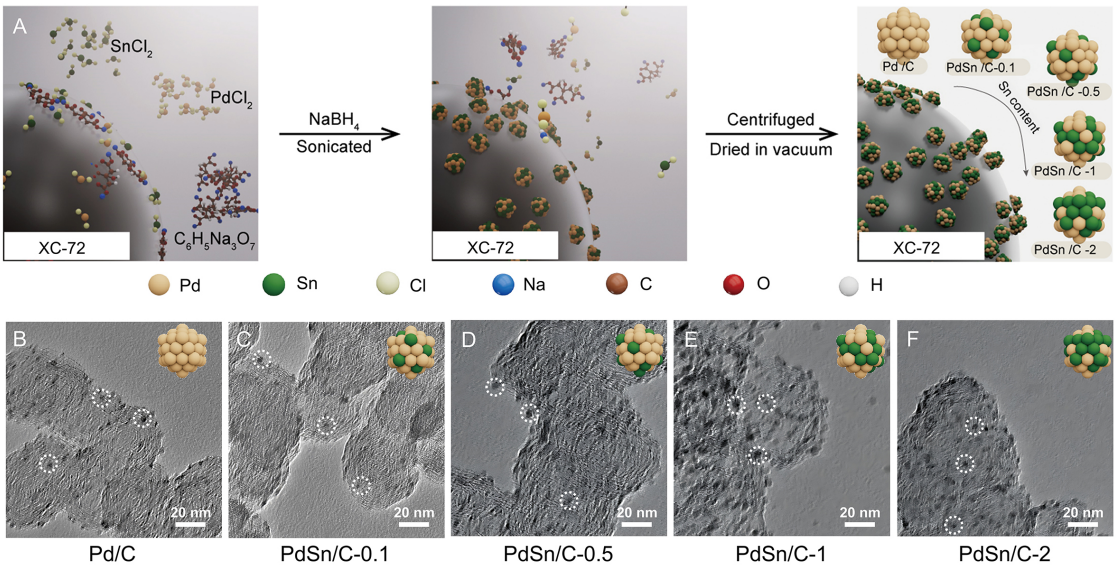

Figure 1. (A) Schematic illustration of preparing PdSn/C-X. TEM images of (B) Pd/C, (C) PdSn/C-0.1, (D) PdSn/C-0.5, (E) PdSn/C-1, and (F) PdSn/C-2.

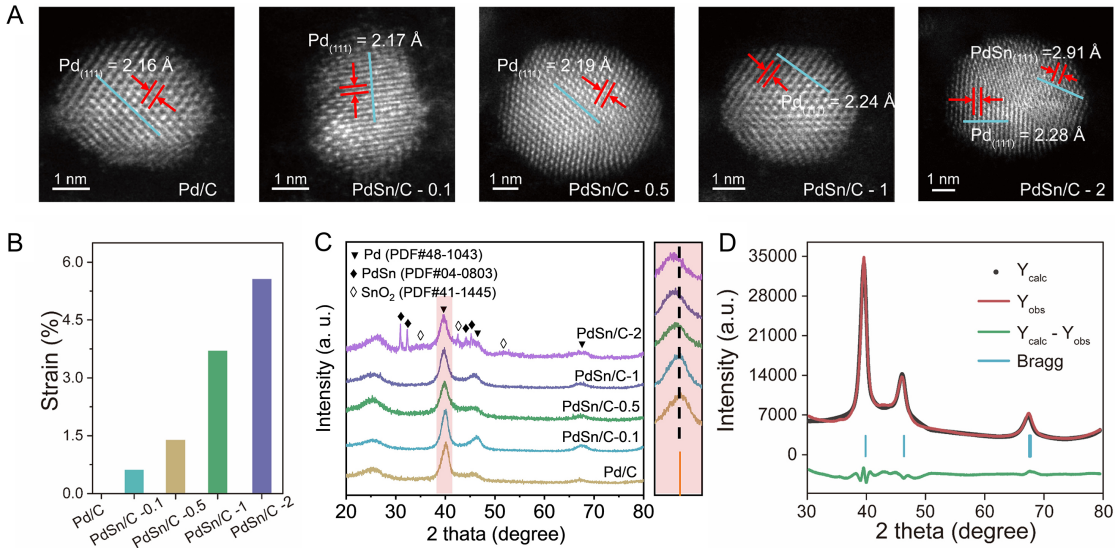

Figure 2. (A) HAADF-STEM images, (B) Lattice stretching ratios, and (C) XRD patterns of Pd/C and PdSn/C-X. (D) XRD profiles and Rietveld refinement fit for PdSn/C-1.

PdSn/C-0.1, 0.5, 1, and 2 [Figure 2B], respectively, by comparing the lattice spacing of (111) plane in PdSn/C-X (d_p) with that on Pd/C (d_s). In addition, the powder XRD patterns of the PdSn/C catalysts are displayed in Figure 2C. All the catalysts exhibit a typical Pd face-centered cubic (fcc) crystal structure of Pd (PDF#46-1043), with peaks around 40.1°, 46.7°, and 68.1°, corresponding to the (111), (200), and (311) reflections, respectively[24]. The broad peak around 25° represents the (002) reflection of carbon from XC-72 carbon support. Notably, the enlarged image in Figure 2C shows a negative shift in the diffraction peak from 40.1° to 39.6° as the Sn contents increase, indicating lattice expansion due to the larger Sn lattice parameter compared to Pd[30,31,33,34]. This phenomenon is consistent with the HAADF-STEM results. Moreover, the Sn-related peaks in the XRD pattern of the PdSn/C-2 [Figure 2C] are clearly visible, while

they are absent in the other samples. This observation can be attributed to the higher Sn content in PdSn/C-2 compared to the other samples, which allows the Sn-related peaks to be more readily detected by XRD. The phase equilibria of the Pd-Sn system are quite complex, with numerous intermediate phases[35]. The alloy formed with a Pd fcc structure can accommodate up to 17% of Sn in the Pd-rich region of the diagram[36,37], leading to the formation of intermetallic phases such as PdSn, Pd_2Sn, $PdSn_2$, or other mixtures. According to previous works[38], the prominent peaks at 30.8° and 32.3° are assigned to the PdSn (111) and (012) (PDF#04-0803), respectively, indicating the presence of the PdSn phase at high Sn doping in PdSn/C-2[30]. Additionally, the distinct peaks at 33.9°, 42.5°, and 51.8°, which correspond to the (101), (210), and (211) reflections of SnO_2 (PDF#72-1147)[39], respectively, were observed on PdSn/C-2, suggesting the formation of SnO_2 phase. As shown in Figure 2D, the Rietveld refinement of the PdSn/C-1 crystal structure (as an example) suggests that a Sn atom substitutes for a Pd atom in the Sn-doped Pd-based catalyst[40]. As expected, these findings indicate that the strain state of PdSn/C-X can be tuned by adjusting the Sn content.

Recent studies suggest that the highest occupied electronic states up to the Fermi level serve as electronic descriptors for electrocatalytic activity[41], as they influence the adsorption and desorption characteristics of reactants and intermediates. Therefore, we conducted density of states (DOS) simulations for the active Pd center using DFT (see Supplementary Material) to understand how strained structures affect surface adsorption behavior [Supplementary Figure 3A]. The Pd d-band center shows a strong correlation with tensile strain [Supplementary Figure 3B], and its value decreases toward the Fermi level as tensile strain increases. According to the d-band theory of metal-adsorbate interactions, this change in d-band electron density has significant catalytic implications[42]. A higher local average of the d-band electron energies (ε_d) near the Fermi level results in a stronger binding strength between the active site and adsorbates[43]. However, if ε_d is too low, the reactants struggle to adsorb, while a high ε_d causes strong adsorption of intermediates, leading to catalyst poisoning[44]. Therefore, an optimal ε_d level accelerates the absorption of reaction intermediates at the active site and promotes the subsequent oxidation phase during the EOR, thereby enhancing catalytic performance.

The surface chemical compositions of PdSn/C catalysts were further analyzed by XPS, using the C1s peak at 284.8 eV for calibration. The survey spectra [Supplementary Figure 4A] confirm the presence of Pd, Sn, and C. High-resolution spectra of Pd 3d for PdSn/C-0.1 to 2 [Supplementary Figure 4B] were deconvoluted into four peaks around 335.9, 337.4, 341.7, and 344.9 eV, corresponding to Pd(0)$3d_{5/2}$, Pd(II)$3d_{5/2}$, Pd(0)$3d_{3/2}$, and Pd(II)$3d_{3/2}$[11], respectively. The high-resolution spectra of Sn 3d [Supplementary Figure 4C] show four peaks around 485.6, 493.9, 487.5, and 495.8 eV, corresponding to Sn(0)$3d_{5/2}$ Sn(IV)$3d_{5/2}$, Sn(0)$3d_{3/2}$, and Sn(IV)$3d_{3/2}$, respectively. Notably, the Pd(0)$3d_{5/2}$ peak shifts to lower binding energy with increasing Sn content, indicating significant electron transfer to Pd. In addition, the proportions of Pd(0) for PdSn/C-0.1, 0.5, 1, and 2 were calculated to be 67.3%, 43.1%, 40.9%, and 46.3%, respectively, based on the peak areas of Pd(0) in Supplementary Figure 4B. The higher proportions of Pd(0) at high Sn content (PdSn/C-2) owes to SnO_2 formation, which hinders Pd oxidation and increases the Pd(0) proportion, demonstrating that Sn incorporation influences Pd valence states due to its oxyphilic properties[31]. Supplementary Figure 4D shows the high-resolution spectra of the O1s region on PdSn/C. The fitted peaks at 532.2, 533.7, and 535.7 eV can be attributed to lattice O from SnO_x, OH^- species, and O from adsorbed H_2O[45,46], respectively. In particular, the proportions of OH^- on PdSn/C-0.1, 0.2, 1, and 2 were calculated to be 16.9%, 26.2%, 36.9%, and 37.2%, demonstrating the increased Sn in PdSn/C promotes OH^- species formation which enhances resistance to CO poisoning. These findings, combined with strain effects, indicate that Sn content modulates tensile strain and chemical states on the surfaces of PdSn/C-X catalysts, providing a basis for enhancing EOR.

Catalytic performance of PdSn/C for EOR

The electrocatalytic performance of the as-prepared PdSn/C catalysts was thoroughly evaluated. Before EOR testing, the CV curves of PdSn/C and Pd/C catalysts were recorded in a N_2-saturated 1.0 M KOH solution [Figure 3A]. The observed cathodic peak around 0.7 V during the backward scans is attributed to the reduction of the Pd oxide layer. Notably, the cathodic peaks of PdSn/C-0.1, 0.5, 1, and 2 are at 0.70, 0.69, 0.71, and 0.73 V (inset in Figure 3A), indicating a more positive peak potential compared to Pd/C (0.68 V). This shift implies the desorption of oxygenated species from their surfaces[15]. Based on the reduction peak area and the Pd content on the working electrode, the ECSAs of PdSn/C-0.1, 0.5, 1, 2, and Pd/C were calculated to be 38.6, 48.5, 104.3, 72.3, and 4.0 m^2/g_{Pd} [Supplementary Figure 5A], respectively. The ECSA of PdSn/C initially grows and then decreases as the Sn content increases. The initial increase is attributed to the enhanced lattice expansion in PdSn/C-0.1 to 1, which activates additional Pd sites. However, the presence of the intermetallic PdSn phase reduces the number of active Pd sites[31]. The electrocatalytic activities of these catalysts for EOR were assessed through CVs recorded in 1.0 M KOH + 1.0 M ethanol solution. Figure 3B shows two typical oxidation peaks in the forward and backward scans, representing the oxidation of ethanol and carbonaceous intermediates, respectively. As shown in Figure 3C, to compare the activities, mass and specific activities were determined by normalizing the peak current densities of ethanol oxidation to the mass of Pd and the ECSAs, respectively. PdSn/C-1 exhibits significantly higher activity (8,452.3 mA/mg_{Pd} or 8.1 mA/cm^2) than PdSn/C-0.1 (2,212.6 mA/mg_{Pd} or 3.7 mA/cm^2), PdSn/C-0.5 (2,536.3 mA/mg_{Pd} or 5.7 mA/cm^2), PdSn/C-2 (3,031.9 mA/mg_{Pd} or 4.1 mA/cm^2), and Pd/C (246.8 mA/mg_{Pd} or 4.6 mA/cm^2), outperforming most of Pd-based catalysts reported in previous studies [Supplementary Table 2]. Figure 3C illustrates a clear "volcano" trend in activity with varying Sn/Pd ratios, reflecting the trend observed in ECSAs. This result indicates that incorporating Sn into Pd-based catalysts significantly improves the catalytic activity by altering the Sn/Pd ratio.

Furthermore, the catalytic kinetics were investigated using linear sweep voltammetry (LSV) and electrochemical impedance spectroscopy (EIS) techniques. As shown in Supplementary Figure 5B, PdSn/C-1 exhibits a significantly lower onset potential (0.63 V) compared to other catalysts (inset of Supplementary Figure 5B), indicating enhanced kinetics for ethanol oxidation. The Tafel slopes increase in the following order: PdSn/C-1 < PdSn/C-2 < PdSn/C-0.5 < PdSn/C-0.1 < Pd/C [Supplementary Figure 5C]. The smallest Tafel slope (175.02 mV dec^{-1}) for PdSn/C-1 suggests the lowest overpotential and fastest reaction kinetics in EOR. Moreover, the EIS results [Supplementary Figure 5D] reveal that PdSn/C-1 has the smallest diameter of the Nyquist plots, demonstrating the lowest charge transfer resistance (R_{ct}, R_{ct} = 83 Ω; see details in Supplementary Table 3) and enhanced reaction kinetics for EOR due to the optimized Sn doping. To assess the long-term catalytic durability of PdSn/C catalysts, chronoamperometry (i-t) tests were conducted at 0.92 V *vs.* RHE for 5,000 s in an N_2-saturated 1.0 M KOH solution containing 1.0 M ethanol [Figure 3D]. PdSn/C-1 exhibits the slowest decay in current density, with a mass activity of 573.9 mA/mg_{Pd} at 5,000 s, outperforming the other catalysts and indicating excellent electrocatalytic durability. Additionally, the stability of PdSn/C-1 was evaluated through extended CV sweeps for 1,500 cycles [Supplementary Figure 6A]. The current density of the forward peaks from the CVs is depicted in Supplementary Figure 6B. Initially, the peak current density increased then decreased with the number of scans, consistent with previous studies[12,47]. Even after 1,500 cycles, the peak current density maintains a mass activity of 1,600 mA/mg_{Pd}, which is much higher than that of Pd/C, indicating good durability. The observed decrease in mass activity during the cycles may be attributed to the partial detachment of the catalyst from the GCE [Supplementary Figure 6C]. Further characterization of PdSn/C-1 was conducted after 1,500 cycles. As shown in Supplementary Figure 7, PdSn/C-1 exhibits a similar particle distribution, size, composition, and crystal structure compared to its state before EOR, confirming its structural stability during the EOR. Overall, the superior performance of PdSn/C-1 is attributed to Sn doping, which modulates the tensile strain and optimizes the adsorption energy of key intermediates, facilitating EOR.

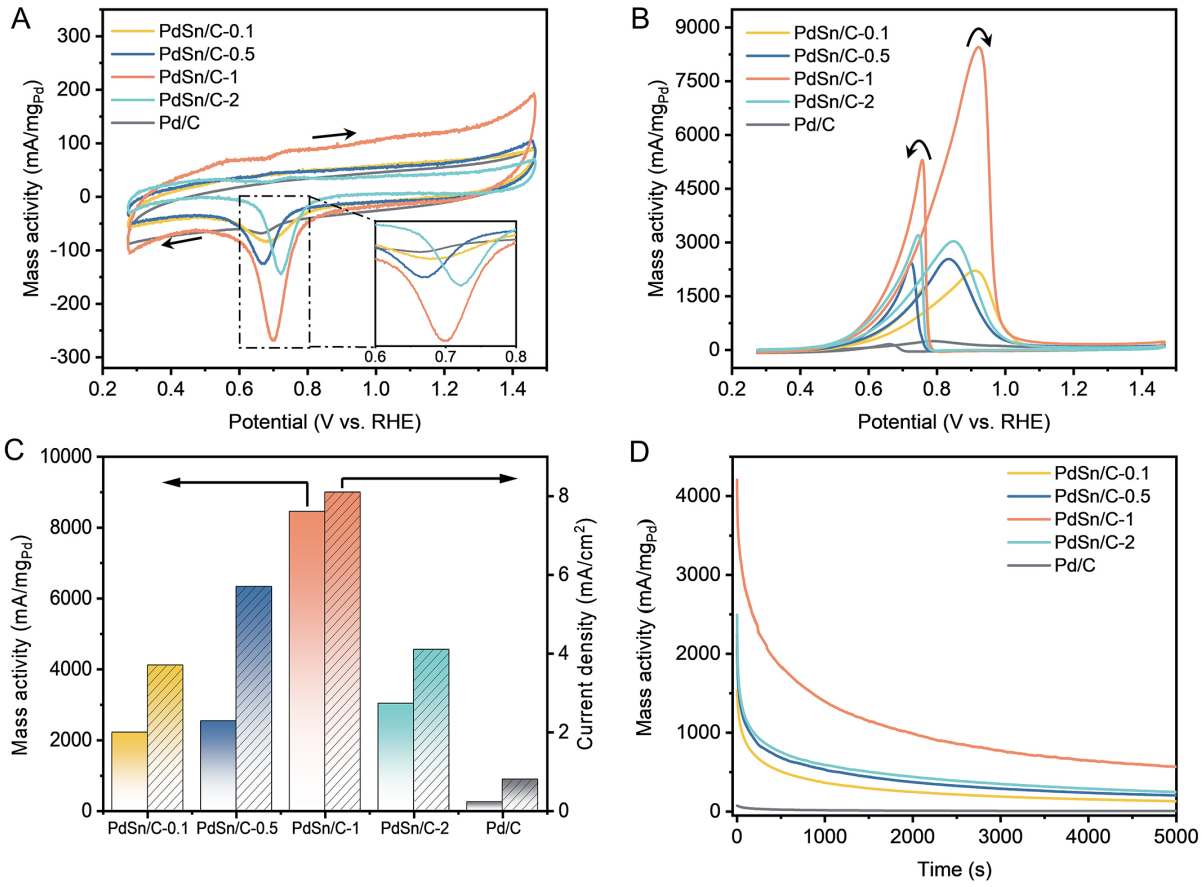

Figure 3. CV curves of Pd/C and PdSn/C-X in (A) 1.0 M KOH solution (inset: the magnified view of reduction peaks) and (B) 1.0 M KOH with 1.0 M ethanol solution. (C) Summarized mass activities (left) and specific activities (right) of Pd/C and PdSn/C-X. (D) i-t measurements at -0.24 V of Pd/C and PdSn/C-X in 1.0 M KOH + 1.0 M ethanol solution.

Finally, electrochemical CO stripping tests were performed on the PdSn/C catalysts to evaluate their capability for removing carbonaceous intermediates. CO stripping voltammograms were obtained by applying a voltage of 0.27 V to the working electrode for 20 min in a CO-saturated 1.0 M KOH electrolyte solution. As shown in Supplementary Figure 8, peaks at 0.88 and 1.08 V in all curves correspond to CO stripping, involving the oxidation of adsorbed CO and its intermediates according to the literature[48-50]. CO adsorbed on the catalysts was nearly completely removed after one scan between 0.27 and 1.47 V. The onset potentials of CO stripping for PdSn/C-0.1, 0.5, 1, and 2 (marked in Supplementary Figure 8) are downshifted by 0.12, 0.15, 0.23, 0.20 V, respectively, from that of Pd/C (at 0.78 V), indicating a reduced tendency for CO poisoning. In addition, among the catalysts with varying Pd/Sn ratios, the PdSn/C-1 catalyst exhibits the largest CO oxidation/removal peak area and the most negative onset potential for CO stripping, suggesting easy CO removal and an effective enhancement of CO tolerance with Sn incorporation[24,25,51]. Notably, appropriately doped Sn, as seen in PdSn/C-1, demonstrates superior CO tolerance, thereby enhancing the catalyst's performance.

Mechanistic investigation of PdSn/C-1 for EOR

To gain insights into how the metal composition of the catalysts affects reaction pathway selectivity during EOR, we conducted *in situ* ATR-SEIRAS studies using PdSn/C-1 and Pd/C catalysts in 1.0 M KOH solution containing 1.0 M ethanol. The spectra obtained during the positive potential sweep for the Pd/C catalyst are

shown in Figure 4A. The appearance of the CO band at 1,800 cm^{-1} within the voltage range of 0 to 1.3 V indicates that the catalyst is capable of undergoing C-C bond cleavage, resulting in the predominance of bridge CO adsorption on the Pd sites[52-54]. This suggests the presence of intermediates via the C1 pathway[55]; however, the adsorbed CO may lead to significant poisoning, hindering the catalytic process. Thus, the C2 pathway dominates during catalytic processes on the Pd/C catalyst, as evidenced by the peaks around 1,420 cm^{-1}, which are assigned to the stretching vibration of CH_3COO^-[56].

However, the PdSn/C-1 catalyst exhibits no adsorbed CO on its surface [Figure 4B] due to the Sn introduction. Notably, a distinct CO_2 adsorption peak emerges, and its intensity increases with potential. Peaks around 2,980 cm^{-1}, assigned to the vibrational characteristics of C-H_x fragments from the methoxy group of ethanol remaining on the catalyst surface after C-C bond cleavage[57], are observed on PdSn/C-1 (right in Figure 4B) but not on the Pd/C catalyst (right in Figure 4A). These results indicate that ethanol electrooxidation on PdSn/C-1 primarily yields CO_2 through the C1 pathway via C-C bond cleavage. Additionally, the strong vibration of H_2O at 1,620 cm^{-1} on PdSn/C-1 (absent on Pd/C) implies the production of abundant OH^- species on oxyphilic Sn for the oxidation removal of *CO[31,58], resulting in significant catalytic activity. Furthermore, a weak peak around 1,400 cm^{-1} was observed in Figure 4B, which can be deconvoluted into two peaks at 1,402 and 1,394 cm^{-1} [Supplementary Figure 9A] attributed to acetate and carbonate[55], respectively. Thus, despite the limitation of intensity, the C1 selectivity (η, in %) was approximately quantified using $\eta = C_{carbonate}/(C_{carbonate} + C_{acetate}) = 6A_{1394}/(6A_{1394} + 4A_{1402} \times 2.2) \times 100\%$[31], where A_{1394} and A_{1402} are the peak areas at 1,394 and 1,402 cm^{-1}, 6 and 4 refer to the number of electrons transferred per one of carbonate and acetate, respectively, and 2.2 is the ratio of the absorbance coefficient per mole of carbonate and acetate. As shown in Supplementary Figure 9B, the η of PdSn/C-1 reached approximately 35.1%, indicating a significant C-C cleavage ability. In summary, the C1 pathway involves the dissociation and adsorption of ethanol, leading to the splitting of the C-C bond and generating hydrogen-rich C1 fragments that undergo complete oxidation without forming toxic intermediates[52].

The EOR mechanism is complex, generally involving C1 and C2 reaction pathways with various surface intermediates[59,60]. To elucidate the reaction mechanism of EOR, we conducted DFT simulations to evaluate the adsorption energy of the Pd (111) surface (as considered according to the XRD results) toward the intermediates during EOR [Supplementary Figure 10]. The free energy profiles of EOR leading to C2 (CH_3COO^-) and C1 (CO_2) products on the surface of Pd are shown in Figure 5A. When comparing the C1 and C2 pathways, they share the same process before *CH_3CO, but differ in whether the *CH_3CO intermediate is dehydrogenated to *CH_2CO or oxidized to *CH_3COOH. The free energy differences between *CH_3CO and *CH_3COOH (ΔG_1) and between *CH_3CO and *CH_2CO (ΔG_2) are 0.24 and 0.44 eV, respectively, which are the highest in their respective pathways. Therefore, ΔG_1 and ΔG_2 not only decide the pathway but also determine the EOR rate. Furthermore, to investigate the effect of tensile strain on the reaction pathway and rate of the Pd-based catalysts, we calculated ΔG_1 and ΔG_2 at various tensile ratios and summarized their deviation (ΔG, $\Delta G = \Delta G_2 - \Delta G_1$) in Figure 5B. ΔG reflects the EOR pathway, favoring the C1 pathway when $\Delta G < 0$, and the C2 pathway when $\Delta G > 0$. For Pd without strain, the C2 product predominates due to a lower ΔG_1 compared to ΔG_2. As the tensile strain increases from 0% to 10%, ΔG decreases from 0.24 to -0.18 eV and then increases to 0.06 eV, achieving the minimum at a tensile strain of 5%. Additionally, ΔG_2 of Pd with a 5% tensile strain is the lowest (0.45 eV) via the C1 pathway compared to other tensile strains. These results indicate that the reasonable modulation of tensile strain not only regulates the EOR process via the C1 pathway by lowering the ΔG but also accelerates the reaction kinetics by decreasing ΔG_2.

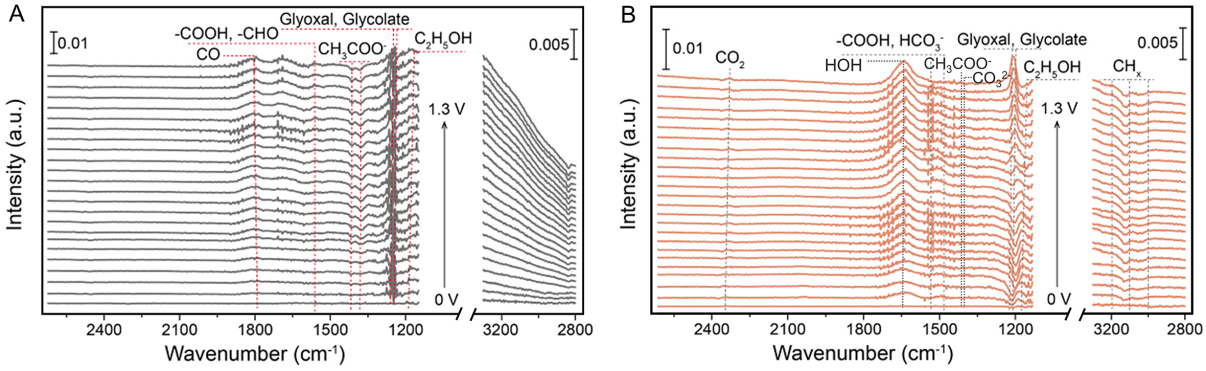

Figure 4. *In situ* ATR-SEIRAS spectra of (A) Pd/C and (B) PdSn/C-1 in N_2-saturated 1 M KOH + 1 M C_2H_5OH solution.

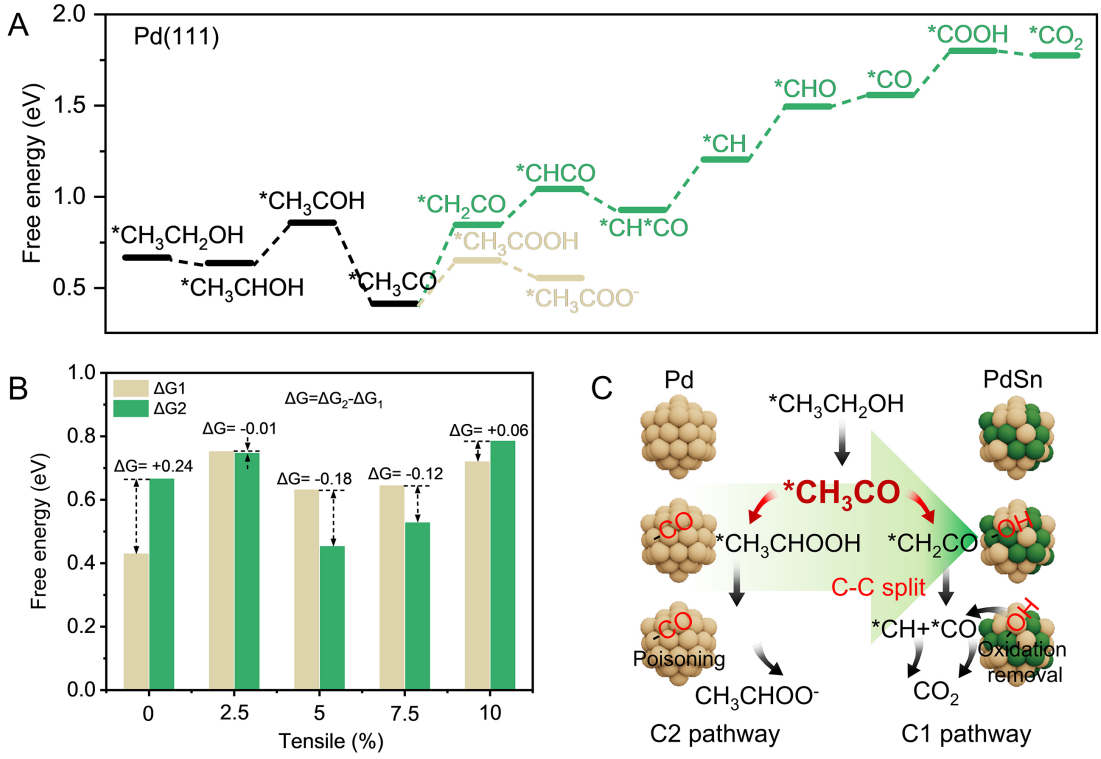

Figure 5. (A) Potential energy diagram for EOR via the C1 (green) and C2 (yellow) pathway on Pd (111). (B) The calculated free energy for ΔG_1 and ΔG_2 on various tensile ratios of Pd (111). (C) Schematic illustration for the EOR process on Pd/C (left) and PdSn/C-1 (right).

Structural analysis, electrochemical evolution, *in situ* ATR-SEIRAS studies, and DFT calculations collectively demonstrate that the incorporation of Sn into the Pd catalyst enhances the catalytic performance for EOR through two pivotal processes [Figure 5C]. First, Sn doping regulates the tensile strain of the Pd crystal, reducing the energy barrier between $*CH_3CO$ and $*CH_2CO$ (ΔG_2) and promoting the C1 pathway. Notably, the optimal ΔG_2 for improved selectivity and kinetics is achieved only with suitable tensile strain (PdSn/C-1). Second, and importantly, the incorporation of Sn provides the oxyphilic sites for OH_{ads} species, facilitating the oxidation removal of CO for enhanced anti-poisoning. These dual contributions underlie the exceptional catalytic performance of PdSn/C-1 in EOR.

CONCLUSIONS

In conclusion, we have developed an efficient co-reduction approach to synthesize PdSn/C catalysts, enabling tunable tensile strain through modulation of Sn content. The PdSn/C-1 catalyst has demonstrated superior catalytic efficacy in EOR, achieving a mass activity of 8,452.3 mA/mg_{Pd}, surpassing that of most Pd-based catalysts. Additionally, Sn incorporation has enhanced the tolerance to CO_{ads} species through oxidation removal. By combining the results of ATR-SEIRAS and DFT calculations, we found that the appropriate Sn component in PdSn/C creates an optimal tensile strain. This strain lowers the reaction energy barrier for the formation of *CH_2CO from *CH_3CO intermediates, a key step in EOR, and favors the C1 pathway through C-C bond cleavage. The strategy of component-regulated strains to enhance catalytic performance in EOR holds promise for the future design of advanced electrocatalysts.

DECLARATIONS

Authors' contributions

Prepared the PdSn/C and performed most of the electrochemical experiments: Tao, Y.
Prepared the PdSn/C and physicochemical characterizations: Cai, Y.
Conducted ATR-SEIRAS experiments: Ding, J.
Performed theoretical calculations: Li, F.
Analyzed the data and wrote and discussed the whole paper: Ma, T.
Supervised students, developed concepts, acquired funding, and revised the manuscript: Chen, R.; Ma, T.; Liang, F.

Availability of data and materials

The data are available upon request from the authors.

Financial support and sponsorship

This work was financially supported by the National Natural Science Foundation of China (Nos. 21871108, U21A20317) and the Program for Innovative Teams of Outstanding Young and Middle-Aged Researchers in the Higher Education Institutions of Hubei Province (No. T201702).

Conflicts of interest

All authors declared that there are no conflicts of interest.

Ethical approval and consent to participate

Not applicable.

Consent for publication

Not applicable.

REFERENCES

1. Nguyen, A. Q. K.; Pham, H. Q.; Huynh, S. T. M.; Huynh, T. T. Milestones of electrocatalyst development for direct alcohol fuel cells. *Adv. Sustain. Syst.* **2023**, *7*, 2300205. DOI
2. Gul Sial MA, Ud Din MA, Wang X. Multimetallic nanosheets: synthesis and applications in fuel cells. *Chem. Soc. Rev.* **2018**, *47*, 6175-200. DOI
3. Zhao, Y.; Setzler, B. P.; Wang, J.; et al. An efficient direct ammonia fuel cell for affordable carbon-neutral transportation. *Joule* **2019**, *3*, 2472-84. DOI
4. Shekhawat, A.; Samanta, R.; Panigrahy, S.; Barman, S. Electrocatalytic oxidation of urea and ethanol on two-dimensional amorphous

nickel oxide encapsulated on N-doped carbon nanosheets. *ACS. Appl. Energy. Mater.* **2023**, *6*, 3135-46. DOI

5. Chen, T.; Xu, S.; Zhao, T.; et al. Accelerating ethanol complete electrooxidation via introducing ethylene as the precursor for the C-C bond splitting. *Angew. Chem. Int. Ed.* **2023**, *62*, e202308057. DOI
6. Luo, S.; Zhang, L.; Liao, Y.; et al. A tensile-strained Pt-Rh single-atom alloy remarkably boosts ethanol oxidation. *Adv. Mater.* **2021**, *33*, e2008508. DOI
7. Wang, Y.; Zheng, M.; Li, Y.; et al. p-d orbital hybridization induced by a monodispersed Ga site on a Pt_3Mn nanocatalyst boosts ethanol electrooxidation. *Angew. Chem. Int. Ed.* **2022**, *61*, e202115735. DOI
8. Monyoncho, E. A.; Steinmann, S. N.; Michel, C.; Baranova, E. A.; Woo, T. K.; Sautet, P. Ethanol electro-oxidation on palladium revisited using polarization modulation infrared reflection absorption spectroscopy (PM-IRRAS) and density functional theory (DFT): why is it difficult to break the C-C bond? *ACS. Catal.* **2016**, *6*, 4894-906. DOI
9. Zhou, X.; Ma, Y.; Ge, Y.; et al. Preparation of Au@Pd core-shell nanorods with fcc-2H-fcc heterophase for highly efficient electrocatalytic alcohol oxidation. *J. Am. Chem. Soc.* **2022**, *144*, 547-55. DOI
10. Luo, M.; Guo, S. Strain-controlled electrocatalysis on multimetallic nanomaterials. *Nat. Rev. Mater.* **2017**, *2*, 17059. DOI
11. Yang, X.; Liang, Z.; Chen, S.; et al. A phosphorus-doped Ag@Pd catalyst for enhanced C-C bond cleavage during ethanol electrooxidation. *Small* **2020**, *16*, e2004727. DOI
12. Huang, W.; Ma, X. Y.; Wang, H.; et al. Promoting effect of $Ni(OH)_2$ on palladium nanocrystals leads to greatly improved operation durability for electrocatalytic ethanol oxidation in alkaline solution. *Adv. Mater.* **2017**, *29*, 1703057. DOI
13. Wang, L.; Liu, Z.; Zhang, S.; et al. In situ assembly of ultrafine AuPd nanowires as efficient electrocatalysts for ethanol electroxidation. *Int. J. Hydrogen. Energy.* **2021**, *46*, 8549-56. DOI
14. Wang, J.; Zhang, G.; Liu, H.; et al. High-performance electrocatalytic reduction of CO_2 to CO by ultrathin PdCu alloy nanosheets. *Sep. Purif. Technol.* **2023**, *320*, 124186. DOI
15. Liu, D.; Zeng, Q.; Hu, C.; et al. Core-shell CuPd@NiPd nanoparticles: coupling lateral strain with electronic interaction toward high-efficiency electrocatalysis. *ACS. Catal.* **2022**, *12*, 9092-100. DOI
16. Wang, H.; Zheng, H.; Ling, L.; et al. Pd metallene aerogels with single-atom W doping for selective ethanol oxidation. *ACS. Nano.* **2022**, *16*, 21266-74. DOI
17. Zhang, Y.; Jang, H.; Ge, X.; et al. Single-atom Sn on tensile-strained ZnO nanosheets for highly efficient conversion of CO_2 into formate. *Adv. Energy. Mater.* **2022**, *12*, 2202695. DOI
18. Feng, C.; Lv, M.; Shao, J.; et al. Lattice strain engineering of Ni_2P enables efficient catalytic hydrazine oxidation-assisted hydrogen production. *Adv. Mater.* **2023**, *35*, e2305598. DOI
19. Cheng, W.; Zhao, X.; Su, H.; et al. Lattice-strained metal-organic-framework arrays for bifunctional oxygen electrocatalysis. *Nat. Energy.* **2019**, *4*, 115-22. DOI
20. He, F.; Zheng, Q.; Yang, X.; et al. Spin-state modulation on metal-organic frameworks for electrocatalytic oxygen evolution. *Adv. Mater.* **2023**, *35*, e2304022. DOI
21. Xu, L.; Fu, B.; Gao, F.; Ma, J. W.; Gao, H.; Guo, P. Strain engineering of face-centered cubic Pd-Pb nanosheets boosts electrocatalytic ethanol oxidation. *ACS. Appl. Energy. Mater.* **2023**, *6*, 2471-8. DOI
22. Zhang, G.; Hui, C.; Yang, Z.; et al. Hydrogen-induced p-d orbital hybridization and tensile strain of PdGa single-atom alloy metallene boosts complete electrooxidation of ethanol. *Appl. Catal. B. Environ.* **2024**, *342*, 123377. DOI
23. Han, S.; Ma, Y.; Yun, Q.; et al. The synergy of tensile strain and ligand effect in PtBi nanorings for boosting electrocatalytic alcohol oxidation. *Adv. Funct. Mater.* **2022**, *32*, 2208760. DOI
24. You, J.; Zhang, Y.; Fan, G.; et al. Component dependent electrocatalytic activity of magnetic bimetallic Pd-Ni nanoparticles for formate oxidation. *Mater. Lett.* **2023**, *343*, 134387. DOI
25. Liang, Y.; Ma, T.; Xiong, Y.; Qiu, L.; Yu, H.; Liang, F. Highly efficient blackberry-like trimetallic PdAuCu nanoparticles with optimized Pd content for ethanol electrooxidation. *Nanoscale* **2021**, *13*, 9960-70. DOI
26. Zou, S.; Ji, Y.; Li, J.; et al. Novel leaflike Cu-O-Sn nanosheets as highly efficient catalysts for the Rochow reaction. *J. Catal.* **2016**, *337*, 1-13. DOI
27. Hidalgo, M. C.; Murcia, J. J.; Navío, J. A.; Colón, G. Photodeposition of gold on titanium dioxide for photocatalytic phenol oxidation. *Appl. Catal. A. General.* **2011**, *397*, 112-20. DOI
28. Maicu, M.; Hidalgo, M. C.; Colón, G.; Navío, J. A. Comparative study of the photodeposition of Pt, Au and Pd on pre-sulphated TiO_2 for the photocatalytic decomposition of phenol. *J. Photoch. Photobio. A. Chem.* **2011**, *217*, 275-83. DOI
29. Primo, A.; Corma, A.; García, H. Titania supported gold nanoparticles as photocatalyst. *Phys. Chem. Chem. Phys.* **2011**, *13*, 886-910. DOI PubMed
30. Salomé, S.; Ferraria, A. M.; Botelho do Rego, A. M.; Alcaide, F.; Savadogo, O.; Rego, R. Enhanced activity and durability of novel activated carbon-supported PdSn heat-treated cathode catalyst for polymer electrolyte fuel cells. *Electrochim. Acta.* **2016**, *192*, 268-82. DOI
31. Ye, N.; Sheng, W.; Zhang, R.; Yan, B.; Jiang, Z.; Fang, T. Interfacial electron engineering of PdSn-NbN/C for highly efficient cleavage of the C-C bonds in alkaline ethanol electrooxidation. *Small* **2024**, *20*, e2304990. DOI
32. Yang, X.; Wang, Y.; Tong, X.; Yang, N. Strain engineering in electrocatalysts: fundamentals, progress, and perspectives. *Adv. Energy. Mater.* **2022**, *12*, 2102261. DOI
33. Wang, W.; Kang, Y.; Yang, Y.; Liu, Y.; Chai, D.; Lei, Z. PdSn alloy supported on phenanthroline-functionalized carbon as highly

active electrocatalysts for glycerol oxidation. *Int. J. Hydrogen. Energy.* **2016**, *41*, 1272-80. DOI
34. Spinacé, E. V.; Linardi, M.; Neto, A. O. Co-catalytic effect of nickel in the electro-oxidation of ethanol on binary Pt-Sn electrocatalysts. *Electrochem. Commun.* **2005**, *7*, 365-9. DOI
35. Okamoto, H. Pd-Sn (Palladium-Tin). *J. Phase. Equilib. Diffus.* **2012**, *33*, 253-4. DOI
36. Dietrich, C.; Chen, S.; Uzunidis, G.; Hähsler, M.; Träutlein, Y.; Behrens, S. Bimetallic Pd/Sn-based nanoparticles and their catalytic properties in the semihydrogenation of diphenylacetylene. *ChemistryOpen* **2021**, *10*, 296-304. DOI PubMed PMC
37. Lanza, R.; Bersani, M.; Conte, L.; et al. Effect of crystalline phase and composition on the catalytic properties of PdSn bimetallic nanoparticles in the PROX reaction. *J. Phys. Chem. C.* **2014**, *118*, 25392-402. DOI
38. Wang, K. W.; Kang, W. D.; Wei, Y. C.; et al. Promotion of PdCu/C catalysts for ethanol oxidation in alkaline solution by SnO_2 modifier. *ChemCatChem* **2012**, *4*, 1154-61. DOI
39. Wu, L.; Yan, H.; Li, X.; Wang, X. Characterization and photocatalytic properties of SnO_2-TiO_2 nanocomposites prepared through gaseous detonation method. *Ceram. Int.* **2017**, *43*, 1517-21. DOI
40. Wei, Z.; Ding, J.; Duan, X.; et al. Enhancing selective electrochemical CO_2 reduction by in situ constructing tensile-strained Cu catalysts. *ACS. Catal.* **2023**, *13*, 4711-8. DOI
41. Li, T.; Zhang, L.; Zhang, L.; et al. Tailoring the chemisorption manner of Fe d-band center with La_2O_3 for enhanced oxygen reduction in anion exchange membrane fuel cells. *Adv. Funct. Mater.* **2024**, *34*, 2309886. DOI
42. Nørskov, J. K.; Abild-Pedersen, F.; Studt, F.; Bligaard, T. Density functional theory in surface chemistry and catalysis. *Proc. Natl. Acad. Sci. USA.* **2011**, *108*, 937-43. DOI PubMed PMC
43. Zhao, C.; Wang, J.; Gao, Y.; et al. D-orbital manipulated Ru nanoclusters for high-efficiency overall water splitting at industrial-level current densities. *Adv. Funct. Mater.* **2024**, *34*, 2307917. DOI
44. Zamora, Z. J. A.; Stevens, M. B.; Gunasooriya, G. T. K. K.; et al. Tuning the electronic structure of Ag-Pd alloys to enhance performance for alkaline oxygen reduction. *Nat. Commun.* **2021**, *12*, 620. DOI PubMed PMC
45. Gao, Q.; Mou, T.; Liu, S.; et al. Monodisperse PdSn/SnO_x core/shell nanoparticles with superior electrocatalytic ethanol oxidation performance. *J. Mater. Chem. A.* **2020**, *8*, 20931-8. DOI
46. Pu, Y.; Celorrio, V.; Stockmann, J. M.; et al. Surface galvanic formation of Co-OH on Birnessite and its catalytic activity for the oxygen evolution reaction. *J. Catal.* **2021**, *396*, 304-14. DOI
47. Ahmed, M. S.; Jeon, S. Highly active graphene-supported Ni_xPd_{100-x} binary alloyed catalysts for electro-oxidation of ethanol in an alkaline media. *ACS. Catal.* **2014**, *4*, 1830-7. DOI
48. Guo, R. H.; Liu, C. F.; Wei, T. C.; Hu, C. C. Electrochemical behavior of CO_2 reduction on palladium nanoparticles: dependence of adsorbed CO on electrode potential. *Electrochem. Commun.* **2017**, *80*, 24-8. DOI
49. Gao, D.; Zhou, H.; Cai, F.; et al. Switchable CO_2 electroreduction via engineering active phases of Pd nanoparticles. *Nano. Res.* **2017**, *10*, 2181-91. DOI
50. Torralba, E.; Blanchard, N.; Cachet-Vivier, C.; Muller-Bouvet, D.; González, J.; Bastide, S. Electrochemical study of carbon dioxide reduction at copper-palladium nanoparticles: influence of the bimetallic composition in the CO poisoning tolerance. *Electrochim. Acta.* **2020**, *354*, 136739. DOI
51. Qiu, L.; Tao, Y.; Ma, T.; Liang, F. Synergistic effect of trimetallic PdCuIn nanoparticles in ethanol and formate oxidation reaction for remarkable catalytic performance. *Energy. Technol.* **2024**, *12*, 2301618. DOI
52. Zhang, Y.; Liu, X.; Liu, T.; et al. Rhombohedral Pd-Sb nanoplates with Pd-terminated surface: an efficient bifunctional fuel-cell catalyst. *Adv. Mater.* **2022**, *34*, e2202333. DOI
53. Demarconnay, L.; Brimaud, S.; Coutanceau, C.; Léger, J. Ethylene glycol electrooxidation in alkaline medium at multi-metallic Pt based catalysts. *J. Electroanal. Chem.* **2007**, *601*, 169-80. DOI
54. Han, C.; Lyu, Y.; Wang, S.; et al. Highly utilized active sites on Pt@Cu/C for ethanol electrocatalytic oxidation in alkali metal hydroxide solutions. *Adv. Funct. Mater.* **2023**, *33*, 2305436. DOI
55. Liang, Z.; Song, L.; Deng, S.; et al. Direct 12-electron oxidation of ethanol on a ternary Au(core)-PtIr(Shell) electrocatalyst. *J. Am. Chem. Soc.* **2019**, *141*, 9629-36. DOI
56. Zhang, J.; Ye, J.; Fan, Q.; et al. Cyclic penta-twinned rhodium nanobranches as superior catalysts for ethanol electro-oxidation. *J. Am. Chem. Soc.* **2018**, *140*, 11232-40. DOI
57. Torrero, J.; Montiel, M.; Peña, M. A.; Ocón, P.; Rojas, S. Insights on the electrooxidation of ethanol with Pd-based catalysts in alkaline electrolyte. *Int. J. Hydrogen. Energy.* **2019**, *44*, 31995-2002. DOI
58. Farsadrooh, M.; Torrero, J.; Pascual, L.; Peña, M. A.; Retuerto, M.; Rojas, S. Two-dimensional Pd-nanosheets as efficient electrocatalysts for ethanol electrooxidation. Evidences of the C-C scission at low potentials. *Appl. Catal. B. Environ.* **2018**, *237*, 866-75. DOI
59. Wu, R.; Wang, L. A density functional theory study on the mechanism of complete ethanol oxidation on Ir(100): surface diffusion-controlled C-C bond cleavage. *J. Phys. Chem. C.* **2020**, *124*, 26953-64. DOI
60. Wang, Y.; Zou, S.; Cai, W. B. Recent Advances on electro-oxidation of ethanol on Pt- and Pd-based catalysts: from reaction mechanisms to catalytic materials. *Catalysts* **2015**, *5*, 1507-34. DOI